Article

Tuning Nanohole Sizes in Ni Hexagonal Antidot Arrays: Large Perpendicular Magnetic Anisotropy for Spintronic Applications

Mohamed Salaheldeen, Miguel Mendez, Victor Vega, Agustín Fernández, and Victor M. Prida

ACS Appl. Nano Mater., **Just Accepted Manuscript** • DOI: 10.1021/acsanm.8b02205 • Publication Date (Web): 03 Apr 2019

Tuning Nanohole Sizes in Ni Hexagonal Antidot Arrays: Large Perpendicular Magnetic Anisotropy for Spintronic Applications

*M. Salaheldeen [¥, Ψ, *], M. Méndez [Ψ], V. Vega [€], A. Fernández [Ψ], V.M. Prida [Ψ, *]*

[¥] Physics Department, Faculty of Science, Sohag University, 82524 Sohag, Egypt.

[Ψ] Depto. Física, Universidad de Oviedo, C/ Federico García Lorca 18, 33007 Oviedo, Asturias, Spain.

[€] Lab. Membranas Nanoporosas, Servicios Científico-Técnicos, Universidad de Oviedo, Campus El Cristo s/n 33006 Oviedo, Asturias, Spain.

Abstract

Perpendicular magnetic anisotropy (PMA) in transition metal thin films offers a pathway for enabling the interesting physics of nanomagnetism and developing wide range of spintronics applications. We demonstrate a simple method to obtain Ni thin films with PMA by depositing them onto nanoporous anodic alumina membranes (NPAAMs), with different pore diameters varying in the range between 32±2 and 93±1 nm. Thus, several sets of Ni antidot arrays thin films have been fabricated with different hole diameter, 35 nm ≤ d ≤ 89 nm, and fixed inter-holes distance, D_{int}, around 103±2 nm, but reducing the edge-to-edge separation between adjacent antidots, ($W = D_{int} - d$), and in two different situations, by considering that W is well above or below the layer thickness, t, of the thin film. The crossover from the in-plane magnetization to out of plane magnetization in a ferromagnetic thin film has been achieved by modifying only the nanopore size of the patterned anodic alumina template and the experimental results were supported by micromagnetic simulations performed with mumax3 code. A dramatic change in the coercivity, H_C, dependence with d and W parameters has been observed with a critical nanohole diameter, d_c, at which the appearance of the perpendicular magnetization is observed. The decreasing of the in-plane coercivity for samples with d > 75 nm is due to the weakened of the in-plane magnetic anisotropy and the rising of the out of plane component. The effective perpendicular magnetic anisotropy energy density for Ni antidot thin film with d = 90 nm and t = 20 nm is around 1.44 erg/cm^2, larger than that obtained by traditional approaches for Ni films with PMA (0.03-0.2 erg/cm^2). These findings point toward antidot thin films as novel routes to engineer the magnetic behavior of ferromagnetic metal with large PMA, which might entail a milestone for future applications in bit patterned magneto-optic perpendicular recording media and spintronic devices.

Keywords: nanoporous anodic alumina templates; thin film antidot arrays; magneto-optic Kerr effect; perpendicular magnetic anisotropy; spintronics

1. INTRODUCTION

Ferromagnetic thin films with perpendicular magnetic anisotropy (PMA) become a key driving force in the progress of magnetic random-access memory (MRAM) devices, spintronic devices and logic chips with high thermal stability.[1–3] The conventional methods for PMA engineering are related to use Ferromagnetic (FM)/oxide interfaces,[4,5] or multilayer structures including two FM or FM/nonmagnetic metal interfaces, [6–8] and amorphous rare earth-transition metal alloys.[9] However, there is still a challenge to enable the large magnetic anisotropy, especially PMA, in commonly used 3d transition metals such as Fe, Co, and Ni (and their alloys) thin films. Here, we propose a Ni thin film with hexagonally antidots arrangement having large PMA that might be of huge importance for nanostructured antidot arrays based spintronics application. The choice of antidot arrays system is governed by its ability for tuning the physical properties of various host-patterned materials by varying the holes parameters in the nanoscale, as they are the nanohole size and their neighboring inter-distance.[10] Moreover, their ability to act as magnonic crystals which - similar to photonic crystals for photons- exhibits a periodic potential for magnons, allowing to modify the spin wave dispersion.[11,12] Thus, antidot arrays systems are promising candidates for applications in the field of spintronics as spin wave filters or spin waveguides.[13,14] In addition, the antidot arrays with PMA easy axis are interesting from the application point of view in superconductor as flux pinning centers.[15–17] Furthermore, many studies used magnetic materials with a perpendicular magnetic anisotropy as host films for the antidot lattices and declared their efficiency for magnetic recording and bit patterned media as compared to unpatterned films.[18,19] Therefore, if high effective PMA could be realized, Ni antidot array structures would be very promising candidates for spin transfer torque magnetic random-access memories (STT-MRAM) and perpendicular bit patterned magnetic storage media applications.[2,3,20] Moreover, the proposed antidot−Ni thin film system is unique in view of the long-standing challenge to promote PMA in

spintronic devices, including materials with a weak spin-orbit coupling (SOC).[21] This fact is very important because of the existence of heavy-ions elements in the system increases the damping constant and strongly reduces the spin diffusion lengths, thus restricting magneto-resistance and preventing low critical currents for magnetization reversal, two initial key factors for STT-MRAM applications.[3,20,21]

Many approaches have been developed to obtain ordered antidot arrays films, such as focused ion beam lithography,[22] holographic lithography,[23] colloidal lithography,[24] and block copolymer self-assembly.[25] Some of these fabrication methods, however, are restricted to laboratory scale applications by expensive procedure or limited patterned areas. Antidot arrays based on nanoporous anodic alumina membranes (NPAAMs) employed as templates, allow obtaining elaborated and reproducible 3D arrangement of self-ordered nanoporous with accurate control on their geometrical parameters, such as the pore size, center-to-center interpores distance and pore length. Normally, the periodical ordering cannot be achieved by using the latter method, but this problem has already been successfully addressed by introducing pre-patterning step before anodization of the alumina surface.[26,27]

In this work, we demonstrate that controlling the geometrical parameters of alumina templates of Ni-antidot arrays thin films can greatly enhance the PMA that is not displayed by continuous Ni thin film, taken as the reference sample. A critical hole diameter, d_c, around of 80 nm has been found, where the crossover of the magnetization from in-plane to out-of-plane occurs. The highest value of the effective perpendicular magnetic anisotropy energy density observed for the Ni antidot thin film with d = 90 nm and t = 20 nm is around 1.44 erg/cm^2, which it is larger than that obtained by traditional approaches for Ni thin films with PMA (0.03-0.2erg/cm^2). These findings point toward the tailoring of large perpendicular magnetic anisotropy for the Ni antidot arrays, which

stands as a hallmark for future bit patterned magneto-optic perpendicular recording media and advanced spintronic applications based on template-assisted deposition techniques.

2. EXPERIMENTAL SECTION

2.1 Synthesis of Nanoporous Alumina Membrane

The pre-patterned masks for the Ni antidot arrays consisting of hexagonally ordered nanoporous alumina membranes were produced through the conventional two-step mild anodization process. [28,29] The continuous Ni thin films were also deposited on a glass substrate, with the same thicknesses than for the antidots samples, in order to compare the obtained results. High purity Al foils (99.999%, Goodfellow, Huntingdon, UK) having 0.5 mm in thickness, were used as a starting material. These Al foils were cleaned by sonication in ethanol and isopropyl alcohols and electropolished at 20 V in perchloric acid and ethanol solution (1:3 vol., 5 °C) for 5 min. Afterwards, the two-step electrochemical anodization procedure of the starting Al foil was performed as reported elsewhere.[29,30] . During the 2nd anodization step, which lasted for 5 h, the nanopores grew following the highly self-ordered hexagonal symmetry pre-patterned engineering during the first anodization process, as schematically shown in figure 1a. In order to obtain the hexagonally self-ordered NPAAM templates with different pore diameter, the samples were submitted to pore widening procedure by chemically etching in 5 wt.% orthophosphoric acid at 30 °C, for several etching times, T_{etch}, which were varied between 5 and 55 minutes. This procedure allowed us to obtain a big amount of NPAAM templates with a wide range of different pore diameters, d_p, varied between 32±2 and 93±1 nm, but keeping constant the interpore distance, D_{int}, to the value of 103±2 nm.

2.2 Fabrication of Ni Antidot Arrays Thin Films

The controlled deposition of the metallic film formed by highly pure metal pieces of Ni (Goodfellow Limited, England, 99.99% purity) was performed by high vacuum thermal evaporation technique (see figure 1b) using an E306A thermal vacuum coating unit (Edwards, Crawley, UK) with an ultimate vacuum better than 4.1×10^{-7} mbar.[29,30,31] The pure Ni metal pieces were put inside a water cooled copper crucible and have been heated by magnetically focused electron beam, 3.1 kV and electric energy 2.7 kW. The evaporated Ni metal was deposited on the top-surface of the NPAAMs, which served as templates to obtain the thin film antidot arrays (figure 1c).[30,31] The layers film thickness was checked by using a quartz crystal controller that monitored the deposition rate of the evaporation source. The distance between the evaporation source to substrate sample holder was fixed at about 18 cm. The deposition rate of Ni metal was around (0.10–0.15) nm/sec, and it was performed with a deposition angle of about 15º measured between the metal target and the normal direction to the sample surface.

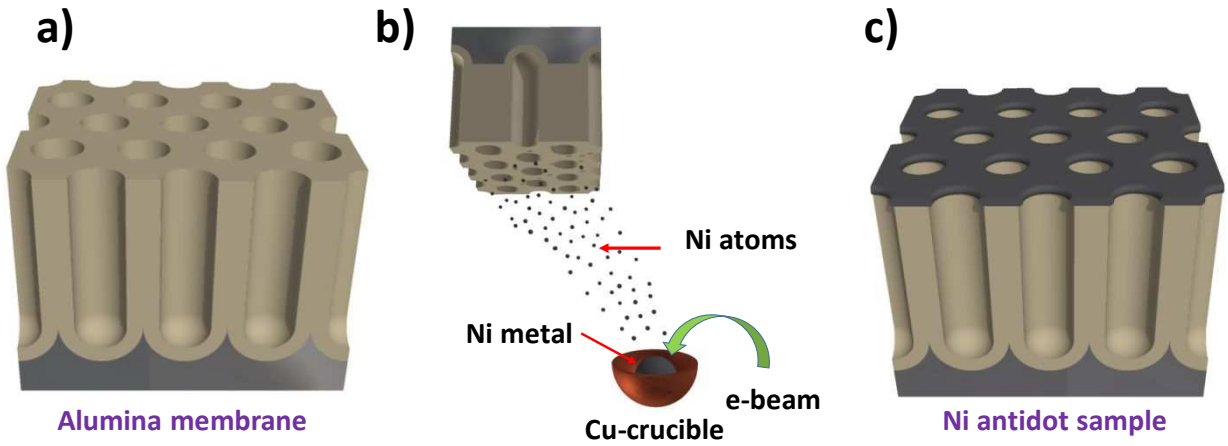

Figure 1: Schematic drawings of a) hexagonally self-ordered nanoporous anodic alumina membrane, NPAAM, as starting substrate, b) Ni vacuum thermal evaporation process on top surface of the NPAAM template and c) Ni antidot thin film sample by replicating the nanoholes structure of the NPAAM template.

2.3 Characterization of Morphological and Magnetic Properties

After the thermal layer evaporation process, all samples were analyzed using scanning electron microscopy (SEM, JSM 5600, JEOL, Akishima, Tokyo, Japan) to measure the nanohole diameter, d, and the inter-holes distance, D_{int}. Figure 2 shows the top view images of nine selected Ni antidot samples having different hole diameter values. For all samples a well-ordered hexagonal arrangement of nanoholes with a constant lattice parameter about 103±2 nm have been observed in good agreement with what is commonly obtained in the patterned alumina substrate after the two-step anodizing procedure in oxalic acid at 40 V.[30] The sample with T_{etch} = 53min. shows the maximum pore diameter of 93 nm and corresponding hole size around of 89 nm that can be achieved for both, the alumina template and Ni antidot thin film samples, respectively (figure 2i). Also, for higher T_{etch} = 55min. the hexagonal pores ordering of the alumina membrane is found to become totally collapsed, as shown in figure 2j.

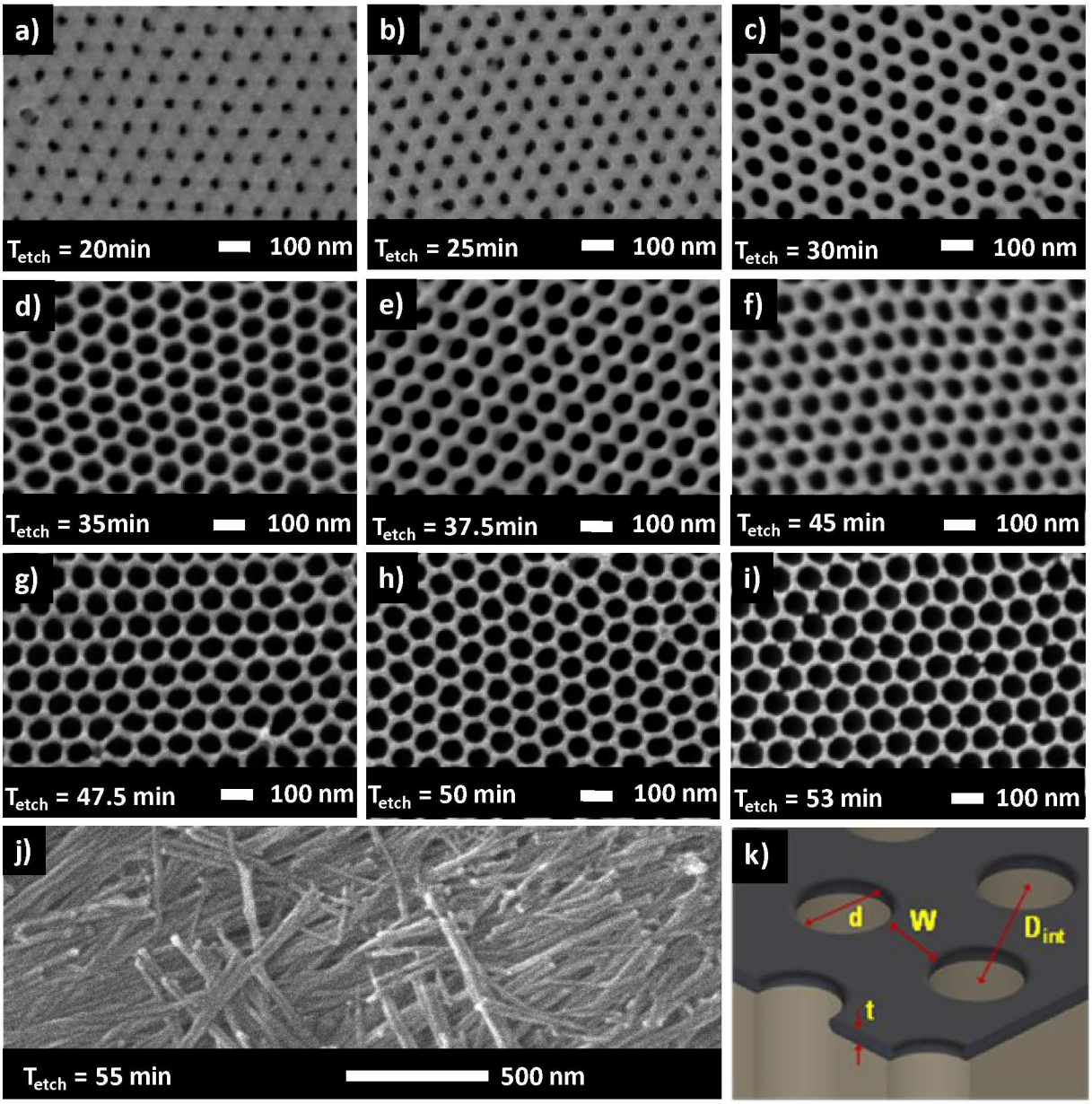

Figure 2: a) to i) SEM images of Ni layer deposited on the top-surface of the NPAAM after being submitted to pore widening process under different chemical etching time, T_{etch}. j) SEM image of the alumina membrane showing the collapse of the hexagonal pores symmetry for T_{etch}. = 55 min. k) 3d sketch of Ni antidot arrays on top surface of the NPAAM, indicating the main morphological lattice parameters of the sample, namely: d = hole diameter, D_{int} = interhole distance, t = thickness, and $W = D_{int}-d$.

Figure 3 summarizes the evolution of the hole diameter, d, and the edge-to-edge distance, W, where ($W = D_{int} - d$), as a function of the etching time for the pores widening. Here, d takes values in the range from 35 ± 3 nm up to 89 ± 1 nm, which is plotted as a function of T_{etch}. Therefore, W decreases from 67 nm down to 14 nm, while D_{int} keeps constant at 103 nm, respectively. A linear relationship is found between d and T_{etch} with an inflection point for T_{etch} = 37.5 min, at which the rate of the pore size increases with etching time changes. Pore wall oxide in the early stage (T_{etch} < 37.5 min., with slope = 1.12) is etched at a higher rate than that in the later stage (T_{etch} > 37.5 min., with slope = 0.84). The retarded rate of chemical etching in the later stage can be attributed to the relatively purer Al oxide nature of the inner pore wall, as compared to the less dense Al oxide of the outer pore wall due to the incorporation of anionic species.[28,32] The linearity of pore diameter increasing with pore widening time has been already previously described for many studies.[28–31] As the center-to-center distance between two adjacent pores (and therefore holes also) remains constant at about 103 nm, the edge-to-edge distance, W, decreases consequently with d increasing, as shown in figure 3b.

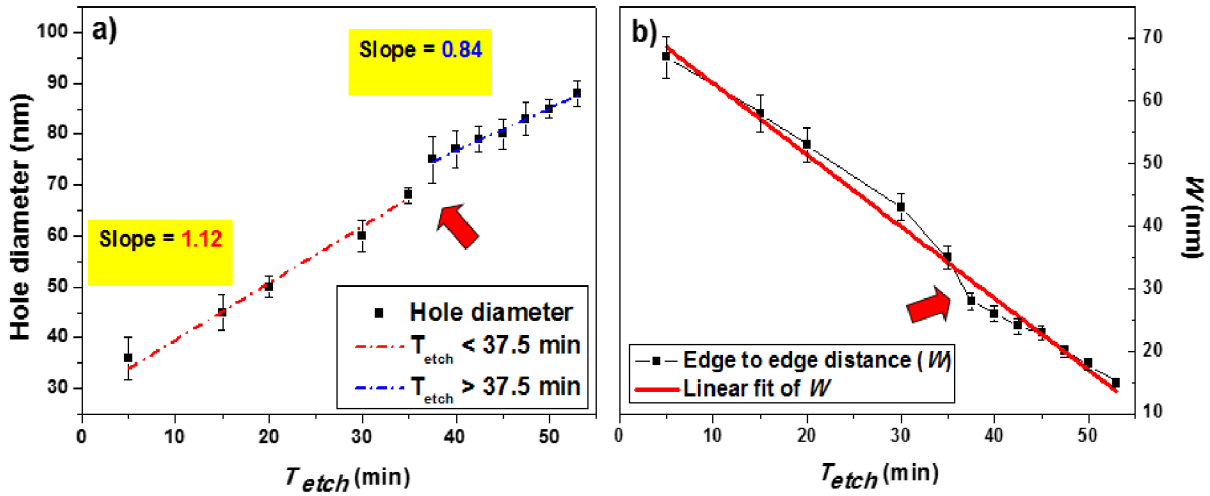

Figure 3: a) Nanoholes size, ***d***; and b) the edge-to-edge distance, ***W***, versus etching time T_{etch} for the Ni thin layer deposited on NPAAM templates. The red arrows indicate the inflection point at T_{etch} = 37.5 min.

In our study, a saturation of the hole diameter seems to occur for the high T_{etch} regime equal to 53 minutes evidenced by the destruction of the hexagonal ordering of the nanoporous structure, as shown in figure 2 j). Indeed, the main reason that may lead to a saturation of the nanohole diameter is the available area between two adjacent holes, which is D_{int}-d, where D_{int} is near to 103 nm. By increasing d and keeping constant D_{int}, this distance is reduced down to its minimum value. Consequently, d reaches a maximum value for a network with a fixed D_{int} parameter, around $d = D_{int} \approx$ 103 nm. Here, the maximum d value reaches ≈ 93 nm, indicating that the stabilization of the hexagonal network is reached up to 90.3% of the maximum value for pores of the alumina membrane and 88 % for Ni antidot thin film with thickness around of 20 nm. This value here achieved is higher than the ones previously obtained with similar techniques.[33–36]

The surface magneto-optic properties of the Ni continuous thin film and antidot array thin films have been obtained making use of a scanning laser Magneto-Optical Kerr Effect (MOKE) magnetometer, NanoMOKE3® (Durham Magneto Optics Ltd., Durham, UK),[30] being able to apply up to 0.125 T by using the quadrupole electromagnet option, or 0.5 T with the dipole electromagnet option.[29,30,31] The NanoMOKE3 magnetometer is matched with p-polarized laser beam and it is sensitive to the Longitudinal-MOKE), (Transversal-MOKE), and (Polar-MOKE), signals, respectively. Complementary bulk magnetic measurements of Ni antidot arrays thin films were carried out by using a vibrating sample magnetometer (VSM-QD-Versalab, San Diego, CA, USA), with applied magnetic fields up to ±3 T, measured at room temperature (RT) and in both, parallel (In-Plane, INP) and perpendicular (Out-of-Plane, OOP), directions to the film plane,

respectively.[29,30] The micromagnetic simulations of Ni antidot arrays with different hole diameter have been performed using the Mumax[3] package software. It allows the calculation of the temporal evolution of the reduced magnetization, $\overrightarrow{\boldsymbol{m}}$, based on the modified Landau-Lifshitz-Gilbert-Slonczewski equation of motion for the magnetization, $\overrightarrow{\boldsymbol{m}}((\vec{r}), t)$. A finite difference discretization permits the magnetostatic field to be estimated as a discrete convolution of the magnetization.[37]

3 RESULTS AND DISCUSSION

For survey the induced PMA by nanoholes of the antidot arrays thin films, we have selected a set of samples having a wide range of hole diameters as summarized in figure 3a and fixed lattice parameters for $\boldsymbol{D_{int}}$ and layer thickness, $\boldsymbol{t}$, of the thin film with averaged values of 103±2 nm and 20 nm, respectively. Also, we divide the antidot samples into two groups according to their $\boldsymbol{W/t}$ ratios, the first group with $\boldsymbol{W > t}$ and the latter group having $\boldsymbol{W \leq t}$.

The surface magneto-optic properties of the Ni antidot thin films were characterized along the INP and OOP directions making use of the MOKE technique. For the INP direction, we selected the INP easy axis, which corresponds to the hysteresis loop with highest $\boldsymbol{H_{C//}}$ and $\mathbf{m_{r//}}$. In figures 4(a, b) there are represented both, the transversal and polar MOKE hysteresis loops of the Ni antidot thin films for the first group of samples with $\boldsymbol{W > t}$. The results are plotted in figure 4 for the antidots with nanohole diameters ranging between 35±3 and 75±2 nm, besides for the unpattern Ni film of same thickness employ as a reference sample. As plotted in figure 4a, the magnetization is initiated to be INP oriented for all samples, as indicated by the large $\mathbf{m_{r//}}$ magnetization and large values of the coercivity. In contract, we detected remnant magnetization near to zero and high

saturating field measured along the OOP orientation (figure 4b). It can also be seen in the figure 4 that the increase in the antidot hole diameter, ***d***, which indicates an increase in the antidot arrays density, leads to an in-plane hysteresis loop with larger coercivity, $H_{C//}$. This fact is consistent with the scenario where the antidots are acting as pinning centers for the displacement of magnetic domain walls.[38]

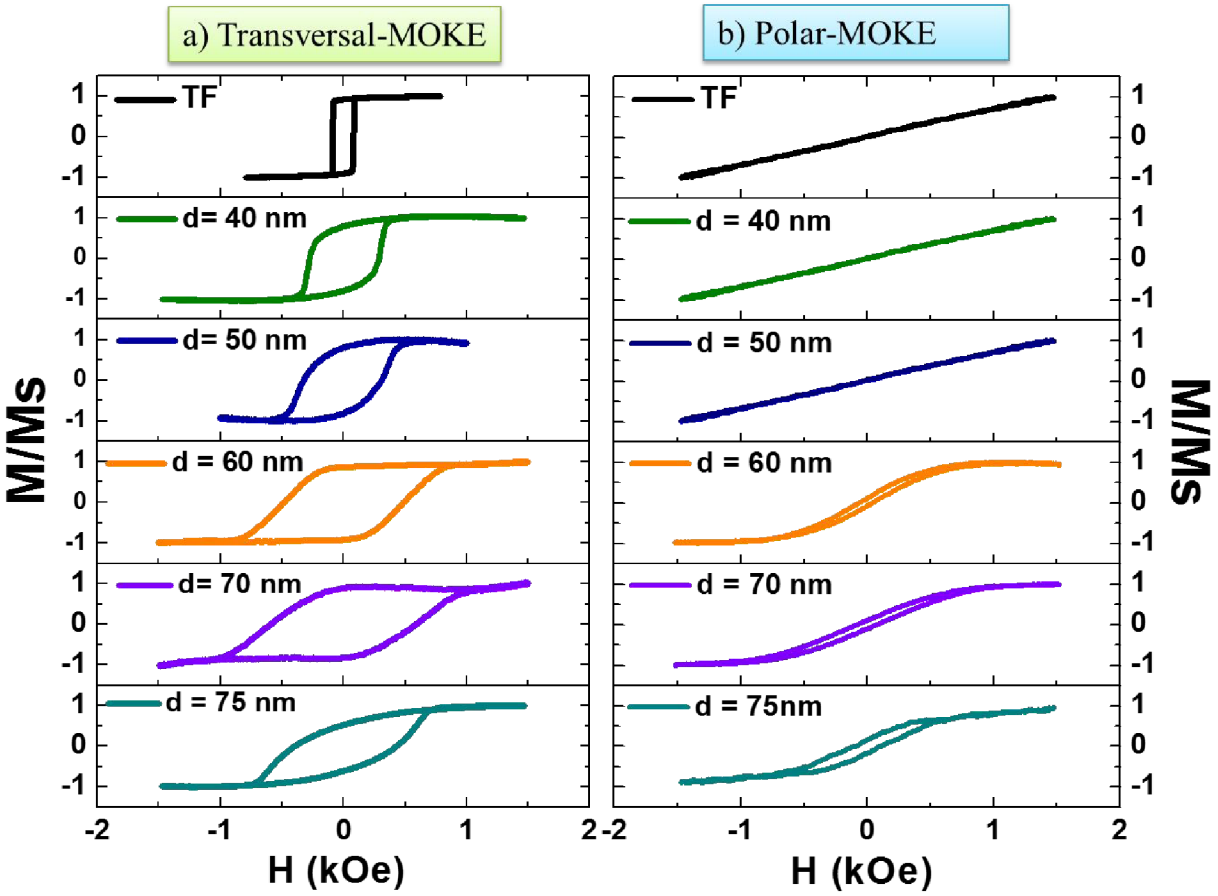

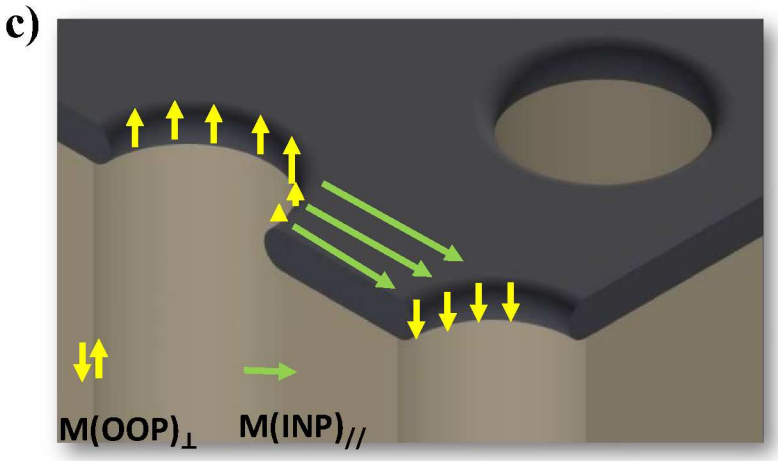

Figure 4: a) Transversal and b) Polar MOKE hysteresis loops for the 20 nm thick continuous Ni thin film (black loop) and Ni antidot arrays samples with different hole diameter ranging from 40 nm up to 75 nm and 103 nm of interpore distance. c) Three-dimensional sketch of the Ni antidot arrays. The arrows indicate the magnetization directions along the magnetic thin films at remanence state for antidot samples with $d < 80$ nm and D_{int} = 105 nm.

The maximum of $H_{C//}$ value of around 590 Oe was obtained for the Ni antidot sample with d= 70 nm, which is approximately 8.5 times larger than the coercivity value of continuous thin film. Also, the enhancement of the out of plane coercivity, $H_{C\perp}$, has been noticed as a consequence of the increase of the hole diameter from zero for the reference sample (continuous thin film) up to $H_{C\perp}$ =77 Oe for the antidot sample with d = 70 nm. This fact indicates that for antidots thin films with large nanoholes diameter, the magnetization does not totally lie in the INP direction, but some magnetization component appeared along the out of the sample plane induced by the holes nanostructuring can be also observed.[39]

For antidot sample with d = 75 nm, a sharp drop of the INP coercivity, $H_{C//}$, and reduced remanence, $\mathbf{m}_{r//}$, has been observed, as $H_{C//}$ and $\mathbf{m}_{r//}$ decreased from 590 to 351Oe and 0.75 to

0.35, respectively. Meanwhile, the OOP coercivity, $\boldsymbol{H_{C\perp}}$, and remanence, $\boldsymbol{m_{r\perp}}$, increase from 77 Oe to 107 Oe and 0.08 to 0.21, respectively. It seems that increased OOP magnetization distribution obtained for this sample with 75 nm of hole diameter is related to the underlying surface morphology of the patterned substrate of the NPAAM. In fact, AD thin films deposited on top-surface of NPAAM templates reproduce the intrinsic surface roughness of the patterned templates,[40–42] but they also develop crescent shape during the thin film deposition process, as sketched in fig. 4c.[43–46] These two morphological features can determine the magnetic anisotropy of the material. Thus, the magnetic moments between nanoholes remain parallel aligned within the film plane, while magnetic moments along the walls of the nanoholes are perpendicularly aligned to the film plane, as schematically shown in fig. 4c. The effect on the magnetization component along the perpendicular direction to the sample surface becomes higher as the nanoholes diameter increases, i.e. $\boldsymbol{W}$ decreases.[34,35,46,47]

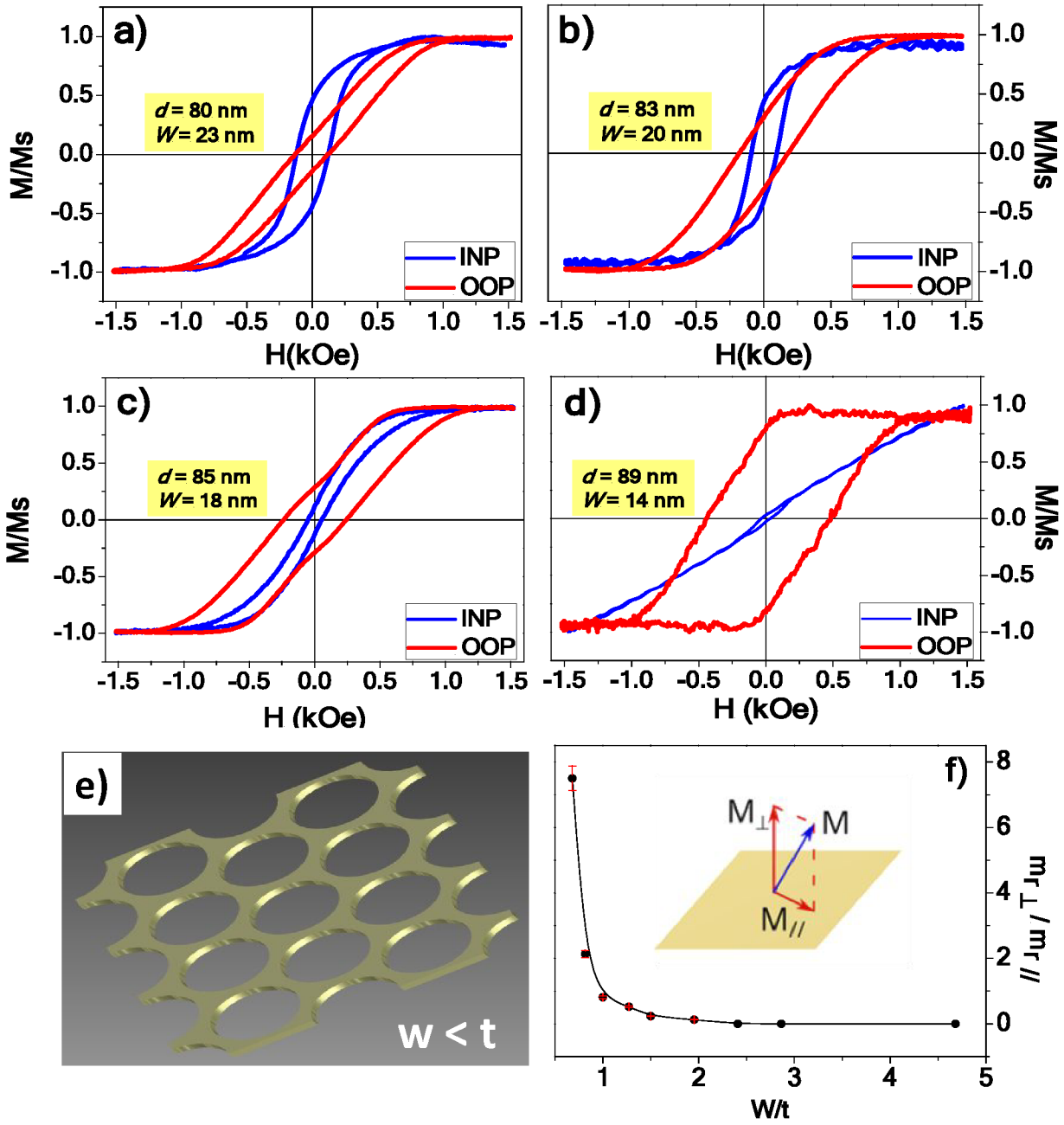

Figure 5: The INP (blue color) and OOP (red color) Kerr hysteresis loops of Ni antidot arrays thin films with 20 nm in layer thickness and different hole diameter of a) 80 nm, b) 83 nm, c) 85 nm, d) 89 nm and 103 nm of interhole distance. e) 3d sketch for antidot arrays with $W \leq t$. f) reduced remanence ratio from OOP to INP directions, $m_{r\perp}/m_{r//}$, calculated from the MOKE hysteresis loops for the Ni antidot samples with different W/t ratio.

Figure 5 shows the INP and OOP hysteresis loops for the second group of Ni antidot samples where $W \leq t$ with hole diameter ranging from 80 to 89±1 nm. Surprisingly, a crossover of the easy magnetization axis from the INP to OOP direction has been detected as shown in graphs 4(c, d). This crossover started with a balance between the INP and OOP coercivity for the sample with nanohole diameter around of 80 nm ($H_C \approx 127$ Oe) for both applied field directions (figure 5a). Then, a balance between the INP and OOP m_r for samples with nanoholes diameter of 83 nm can be observed, together with a dominated OOP coercivity, as shown in figure 5b. Finally, a dominant magnetization component along the perpendicular to the plane of the sample surface has been observed as plotted in figure 5(c, d). From the analysis of the INP and OOP hysteresis loops for a given Ni antidot hole diameter, we calculate the ratio between the component of reduced remanence perpendicular to the sample surface, m_r $(OOP)_{\perp}$, and the reduced remanence component parallel to the film surface, m_r $(INP)_{//}$. When the ratio between $m_{r\perp}/m_{r//} = 0$ means that magnetization is mainly lying in the INP direction, while $m_{r\perp}/m_{r//} \gg 1$ means that magnetization is essentially pointing towards the OOP direction.[21] Accordingly, the antidot sample with the maximum size of hole diameter around of 89±1 nm (i. e.: $W/t << 1$) shows high $m_{r\perp}/m_{r//}$ ratio of 7.5, thus indicating a strong perpendicular anisotropy for this sample. Meanwhile, the other sample showed intermediate perpendicular anisotropy with $m_{r\perp}/m_{r//} = 2$. On the contrary, the continuous thin films and samples with small nanohole diameter show an in-plane magnetic anisotropy with $m_{r\perp}/m_{r//}$ ratio ≈ 0, as plotted in figure 5f.

It should be also of great interest to investigate the dependence of the effective magnetic anisotropy coefficient, K_{eff}, and the effective perpendicular magnetic anisotropy energy density ($Keff \times t_{Ni}$) with varying the size of holes diameter. The effective magnetic anisotropy K_{eff},

determined from the difference between the areas of the INP and OOP hysteresis loops and that can be calculated by the given expression:[30,48]

$$\boldsymbol{K_{eff}} = \mathrm{K_{OOP}} - \mathrm{K_{INP}} = \int_{0-\mathrm{OOP}}^{\mathrm{M_s}} \mathrm{HdM} - \int_{0-\mathrm{INP}}^{\mathrm{M_s}} \mathrm{HdM} \quad (1)$$

Where $\boldsymbol{M}$ is the magnetization, $\boldsymbol{M_S}$ denotes the saturation magnetization and **H** is the applied magnetic field.

A clear trend of $\boldsymbol{K_{eff}}$ depending on the hole diameter can be seen, in figure 6. The larger the INP magnetic surface coverage i.e. continuous thin films and antidot with small $\boldsymbol{d}$, the greater the effective magnetic anisotropy coefficient. This trend can be explained by a simple model based on the influence of nanoholes edge defects, which reduce the value of the INP magnetic anisotropy locally.[44,49,50] The unpatterned Ni thin film shows an INP effective magnetic anisotropy that is mainly due to the shape anisotropy of the sample. The INP $\boldsymbol{K_{eff}}$ decreases with the increase of nanohole diameter, $\boldsymbol{d}$, which means that the hard magnetization axis displayed by the continuous unpatterned thin film that is pointing along the out of plane direction, turns into softer for the antidot samples with larger holes diameter and lower $\boldsymbol{W/t}$ ratios.[48,51] Different "local" shape anisotropy is thus expected, with a stronger contribution of the OOP anisotropy with increasing the size of nanoholes diameter.[48] Navas et al.[48] and Jafaar et al.[52] also reported a decrease in the INP effective anisotropy of Ni continuous thin film from 1.2 x 10^6 erg/cm^3 to 0.4 x 10^6 erg/cm^3 for Ni antidots with largest hole diameter (70 nm), with strong contribution of local perpendicular magnetic anisotropy, but still the magnetization lies along the INP direction, which is ascribed to a positive value of $\boldsymbol{K_{eff}}$. Wherever the critical hole diameter is found to be around $\boldsymbol{d_c} \approx 80$ nm, the value of effective magnetic anisotropy decreased to the lowest value (0.15 x 10^6 erg/cm^3) and a counterbalance between the parallel and perpendicular components of the magnetic anisotropy

contributions takes place. Moreover, a dramatic change in the easy magnetization axis of the sample occurs when the nanohole diameter crossed above its critical size (for a determined value of the ratio $W/t \approx 0.8$ & 0.65, and $d \approx 85$ & 90 nm, respectively), rotating from the INP toward OOP direction (negative values of K_{eff}), when the value of nanoholes diameter overcomes its critical size, $d > d_c$. [34,46]

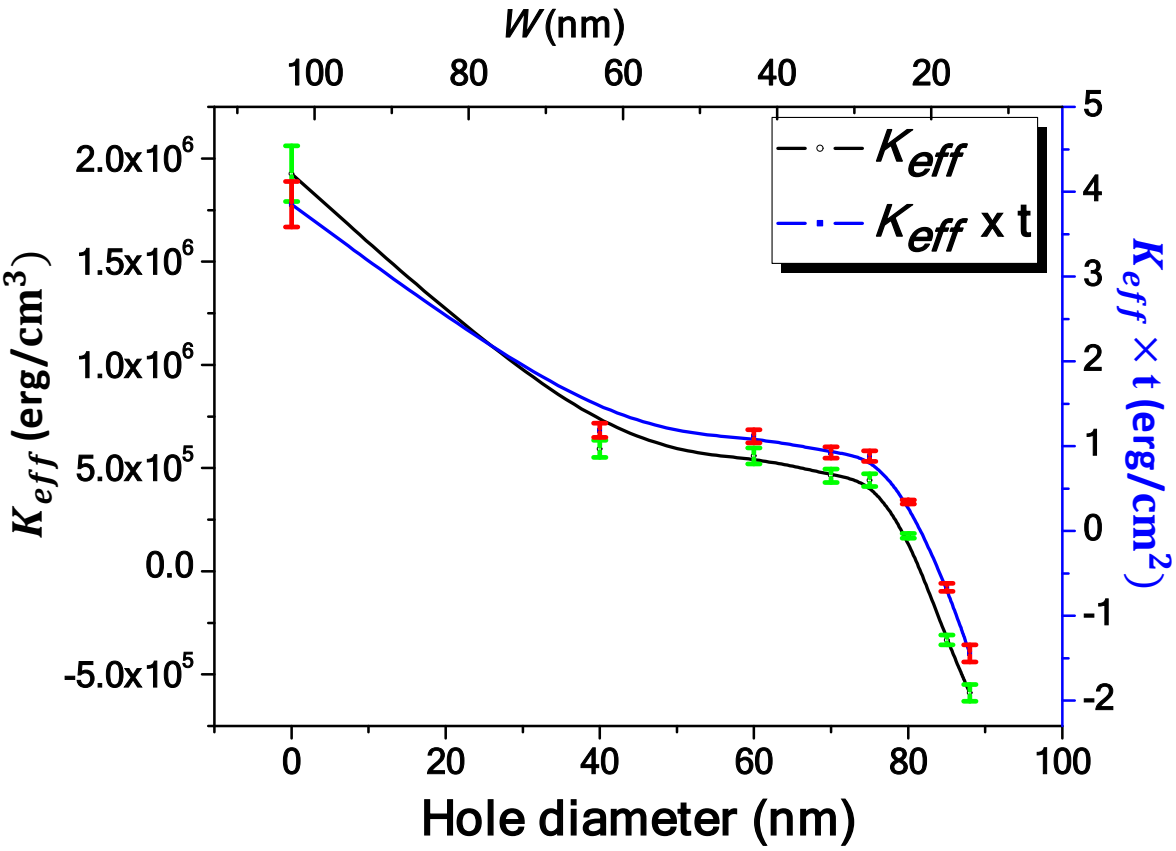

Figure 6: Effective anisotropy, K_{eff}, (left axis), and effective anisotropy energy density, $K_{eff} \times t$, (right axis), as a function of antidot hole diameter (down scale) and the edge-to-edge distance, W, (top scale) for Ni antidot thin film. Negative values of K_{eff} and $K_{eff} \times t$ correspond to antidot samples with perpendicular (OOP) effective anisotropy. The lines are guides to the eye.

The highest value of the effective perpendicular magnetic anisotropy energy density observed for the Ni antidot thin film with d = 90 nm and t = 20 nm is around ($K_{eff} \times t \sim 1.44$ erg/cm^2) , that is more than (7.5-48)-times stronger than that observed for Ni/Pt (0.18 erg/cm^2), or Co/Pt (0.2 erg/cm^2) and Ni/Pd (0.03 erg/cm^2), multilayer thin films with PMA, respectively[7,53,54]. This larger PMA value is also higher than those obtained in Ni/Cu (0.1 to 0.67 erg/cm^2) and Fe/MgO (0.1 erg/cm^2) continuous thin film with thickness 0.1 to 8.5 nm deposited on epitaxial single crystal exhibiting PMA[55-57]. Thus, the high value of the effective perpendicular magnetic anisotropy energy density that has been obtained in this work for the Ni antidot thin film with largest nanoholes diameter, make them as excellent candidates for spintronics applications, bit patterned magneto-optic perpendicular recording media and magnetic sensors based on template-assisted deposition methods.

By studying the complete magnetic behavior of the INP and OOP coercivity of the two groups of samples with d and W that are plotted in figure 7, we can distinguish between two main regimes of antidot densities:

Low-Density Antidot (LD-AD) regime: d < 75 nm $\Rightarrow W$ >28 nm. The antidots array are well separated from each other, and the expected tendency of the in-plane coercivity, $H_{C//} \propto d$, are followed as plotted in figure 7. Also, the OOP coercivity exhibits the same tendency of the INP coercivity with d but with a slow rate, because of the dominating in-plane magnetization and the magnetization reversal occurs by domain walls movement.[58,59]

High-Density Antidot (HD-AD) regime: d > 75 nm $\Rightarrow W$ < 28 nm. When the distance W among antidots array is small, a change in the dependence of the $H_{C//}$ on nanoholes geometry has been shown, as it sharply decreases with d increasing, in contrast to detected for the linear increase in

the LD-AD regime. It is worth noting that the HD-AD regime represents an intermediate state between antidot and dot regimes, as previously reported by other authors.[38,60,61] In this intermediate regime (i.e. HD-AD) the evolution of magnetic parameters such as $\boldsymbol{m_{r//}}$, $\boldsymbol{K_{eff}}$, and $\boldsymbol{H_{C//}}$ changed, as shown in figures 5f, 6 and 7, respectively, in good agreement with previous works.[38,60] This change is an indication of a change in the magnetization reversal mechanism in the antidot samples, which transfers from domain wall propagation to magnetization rotation of single domain structures.[38,60,61] The reduction of the INP coercivity in this antidot regime is mainly due to the reduced magnetic anisotropy for these samples as shown in figure 6. In addition, as $\boldsymbol{d}$ is further increased (i.e. $\boldsymbol{W}$ decreases), the inter-distance between adjacent holes becomes narrower, and the film area that has to be nucleated with a reversed domain is smaller.[38] Consequently, $\boldsymbol{H_{C//}}$ decreases. At the same time, the OOP coercivity is increasing rapidly until equals the value of INP coercivity at $\boldsymbol{W}$ = 22 nm, when the hole diameter reaches the critical size, $\boldsymbol{d_c}$.

It is a remarkable observation the relationship between the critical hole diameter and the characteristic length, $\boldsymbol{R_{crit}}$, since the latter refers to the maximum size of the ferromagnetic material when its magnetization reversal takes place by quasi-uniform magnetization rotation process rather than domain wall displacement. The characteristic length is given approximately by:[62,63]

$$\boldsymbol{R_{crit}} \approx \frac{\sqrt{\boldsymbol{A_{exch}}}}{M_S} \approx 2.5\, \boldsymbol{l_{ex}} \qquad \textbf{(2)}$$

Where $\boldsymbol{A_{exch}}$. is the exchange constant, $\boldsymbol{A_{exch}}$.~10^{-6}erg/cm, $\boldsymbol{M_S}$ is the saturation magnetization, M_S(Ni) = 485 emu/cm^3, and $\boldsymbol{l_{ex}}$ is the exchange length ($\boldsymbol{l_{exch}}$ (Ni) ~ 8.3x10^{-7} cm). Therefore, the estimated value of the characteristic length for Ni is equal to 20.7 nm (about the same order of magnitude than the critical diameter, $\boldsymbol{d_c} \approx$ 22 nm), which ranges within the HD-AD regime, where the magnetization reversal experiences a transition from magnetic domain wall movement (LD-

AD regime), to quasi-uniform magnetization rotation of single domain.[63] Actually, the maximum length, $\boldsymbol{R_{sd}}$ for Ni to be in a single domain is calculated from ($R_{sd} = \frac{36\ \sqrt{A_{exch}K_u}}{\mu_0 M_s^2}$), where K_u is the uniaxial anisotropy constant for Ni.[62] The R_{sd} for Ni is around 25 nm, i.e. the HD-AD regime shows the single domain state. For $\boldsymbol{W}$ = 13 nm i.e. $\boldsymbol{R_{crit}} \approx 1.5\ \boldsymbol{l_{ex}}$ the magnetization reversal can be only carried out by magnetization rotation of single-domain areas, which the magnetic behavior of HD-AD near to magnetic nano islands.[38,60,61] In addition, when the film thickness is larger than the inter-holes distance, the magnetic moments of the single domains rotate towards the OOP direction, thus resulting in an out-of-plane easy magnetization axis.

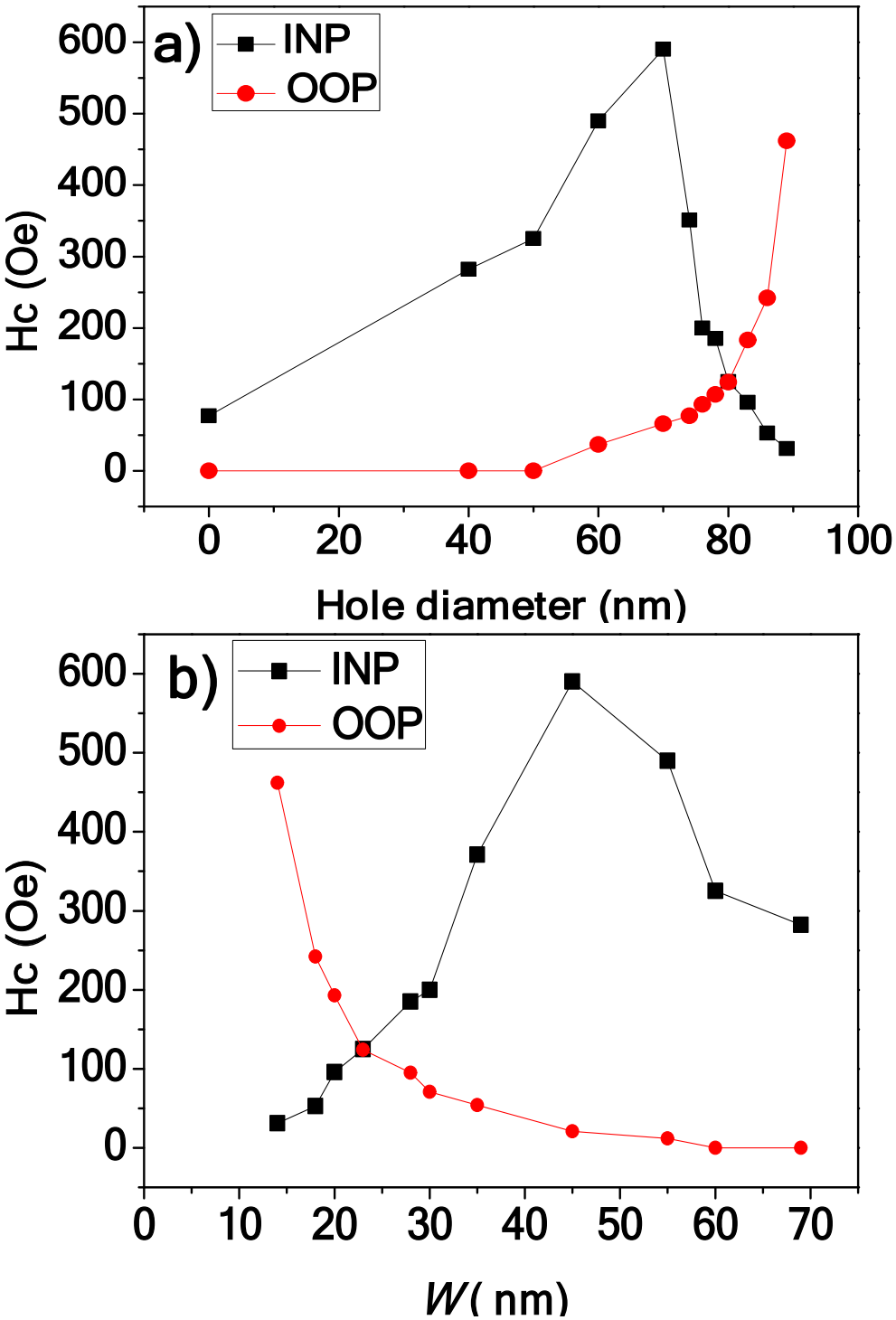

Figure 7: Coercivity, H_C, dependence for the OOP and INP directions of Ni antidot array as a function of a) antidot hole diameter, b) edge-to-edge separation, W.

Micromagnetic simulations of the Ni thin films and the antidot arrays samples were performed using the 3D object-oriented micromagnetic framework by Mumax[3] package with finite element discretization.[37] Under this frame, the ferromagnetic system is divided into cubic cells with a uniform magnetization inside each cell. For the micromagnetic simulations, a grid has been taken as the hexagonally ordered antidots array lattice of 2×2 μm^2 with 512×512×16 cells in the *x*, *y* and *z* axes, respectively, with dimensions for the unit cell along each axis of 3.9 nm (*x*), 3.9 nm (*y*) and 3.125 nm (*z*). The ordered Ni antidot arrays are defined by a layer thickness, $\boldsymbol{t}$ = 20 nm, the interspacing distance between neighboring holes measured center-to-center (105 nm), and the nanohole diameter was varied from 40 to 100 nm. Typical values of the magnetic parameters here employed for Ni were: saturation magnetization $\mathbf{M_S}$(Ni) = 485 emu/cm^3, exchange constant, $\mathbf{A_{exch}}$ (Ni) = 10^{-6} erg/cm^3 and damping coefficient constant of 0.01.[63] Because of the polycrystalline structure of the Ni thin film, the magnetocrystalline anisotropy at RT becomes negligible, so we set this parameter to zero in the simulations. Through the above micromagnetic simulations, it is considered an external magnetic field applied parallel to the film plane in (*x*) and (*y*) directions, as well as in the out of plane direction (*z*), in order to detect the easy magnetization axis (inset figure 8a), ranging from saturation 4500 Oe to -4500 Oe, passing through the remanent state for both, the INP loops and perpendicular to the film plane for the OOP loops.

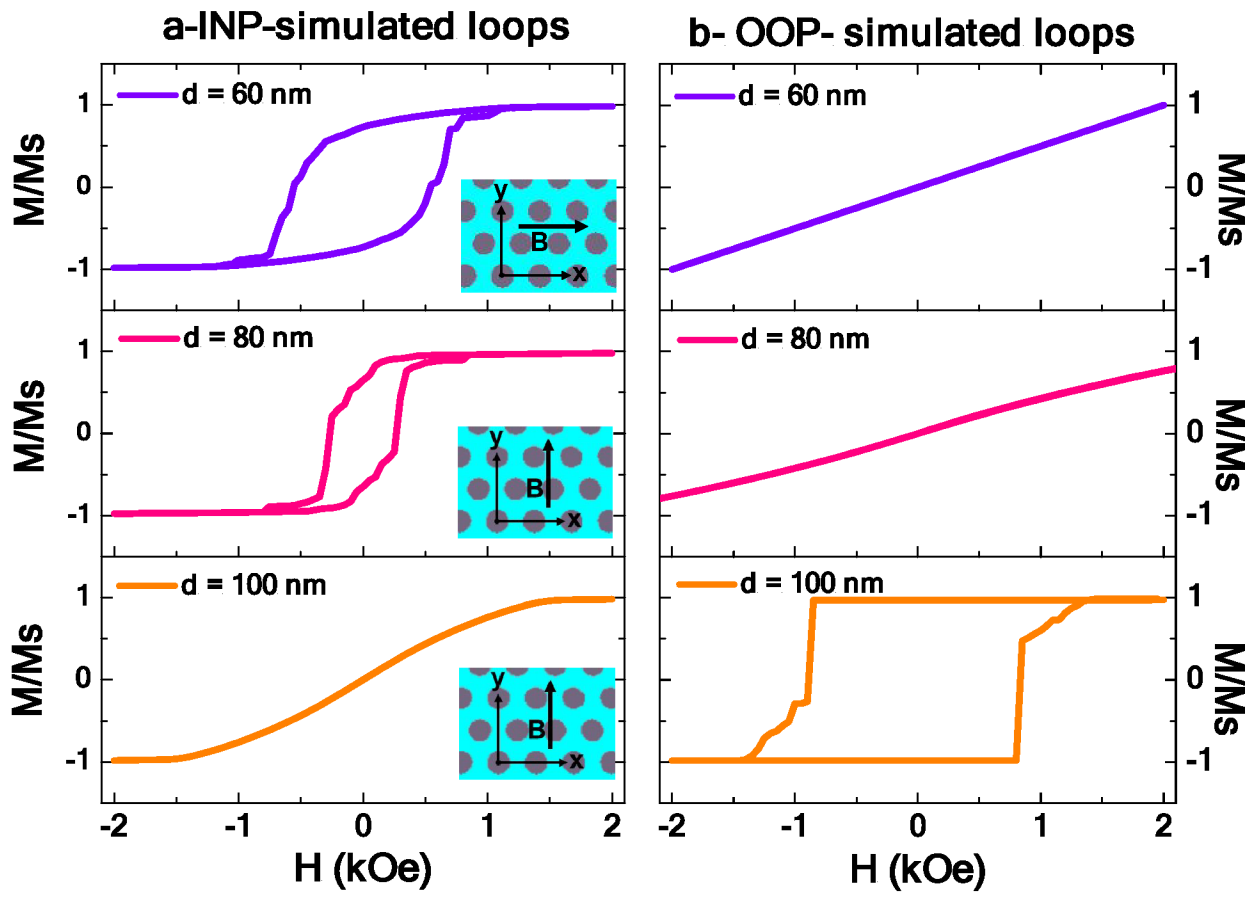

Figure 8: Micromagnetic simulations of hysteresis loops for a) In-plane (inset: 2×2 μm^2 ordered Ni antidot arrays with applied external magnetic field along the *x* or *y* direction as indicated in the pictures) and b) Out of plane directions to the Ni antidot arrays thin film plane and with different holes diameter ranging from 60, 80 and 100 nm, but keeping constant the inter-nanohole distance of 105 nm.

Figure 8 shows selected INP and OOP hysteresis loops for Ni antidot arrays with $W > t$ (blue loops), W near to t (red loops) and $W < t$ (orange loops) obtained by micromagnetic simulations with the above selected parameters. The simulated hysteresis loops match well within the experimentally measured by MOKE. However, the magnetic parameters derived from the

simulated hysteresis loops, such as coercive field and remanence are higher than that extracted from the experimental results. These quantitative differences can be explained in the frame of the micromagnetic model employed for simulations: First, our micromagnetic simulations do not take into consideration thermal disorder effects whereas the experiments were performed at room temperature; second, for saving computational time, the simulations have been performed by considering only a small portion of the whole system corresponding to an area of 2×2 μm^2, while our experimental measurements consider the whole sample dimensions of 2×2 mm^2. Finally, the differences between experimental data and micromagnetic simulations may be explained by the morphological topography (surface roughness of remaining continuous thin layer between the holes), in addition to the presence of microstructural defects in the samples, such as local hexagonally-ordered hole domains separated by boundaries, which are not included in the simulated, ideally ordered flat surface area. Therefore, the value of the critical size for the nanohole diameter, $\boldsymbol{d_c}$, obtained through micromagnetic simulations, at which the magnetization transition from the INP to the OOP occurred, is 100 nm, that is 11 nm larger than the experimental one. For the simulated loop with hole diameter of 100 nm, the value of perpendicular coercivity $\boldsymbol{H_{C\perp}} \sim 820$ Oe is almost twice larger than the experimental value of OOP coercivity, $\boldsymbol{H_{C\perp}} \sim 445$Oe, meanwhile, the $\boldsymbol{H_{C//}}$ is almost zero for both cases. Also, the out of plane reduced remanence obtained from micromagnetic simulations shows a higher value of 0.99 than compared to the experimental one of 0.82 obtained from the measured hysteresis loop of the sample with PMA.

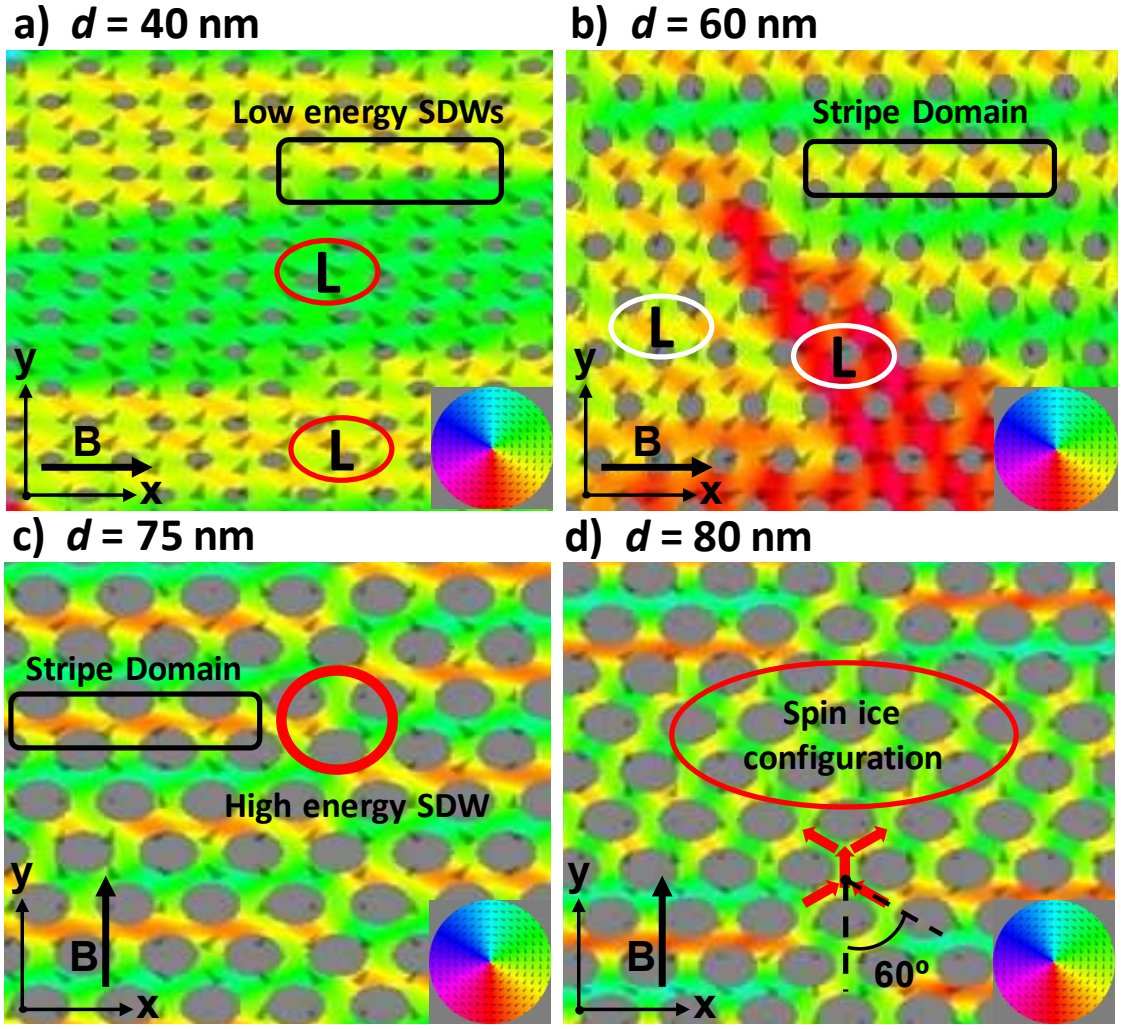

Figure 9: Micromagnetic simulations of magnetic domain structure at remanent state for Ni antidot samples with nanohole diameter, ***d,*** of: a) 40 nm, b) 60 nm, c) 75 and d) 80 nm. The colored maps represent the angle between the INP magnetization component and the *x*-axis or *y*-axis, and the arrows provide a qualitative view of the magnetization orientation.

Figure 9 shows selected micromagnetic simulation images of magnetic domain structure for Ni antidot samples. The images have been taken at remanent state after saturating the samples along the in-plane easy direction. For samples with ***d*** = 40 nm and 60 nm the in-plane easy magnetization

axis lies in the *x* direction (i.e. near neighbor holes) where the highest values of $\boldsymbol{H_C}$ and $\boldsymbol{m_r}$ are obtained. Meanwhile, the hard magnetization axis in these samples lies along the *y* direction (i.e. next near neighbor direction), which shows the lowest values of $\boldsymbol{H_C}$ and $\boldsymbol{m_r}$. The micromagnetic domain structures for d = 40 nm show so-called leaf structure[61], noted as **L** in figure 9a, in order to reduce the magnetostatic energy of the samples. In addition, each two L-structures with different magnetization direction, i.e. different color, are connected with Low energy super domain wall, LE-SDWs.[58] These LE-SDWs are mainly formed when head-to-tail or tail-to-head configurations of the average magnetization vector take place with low stray field divergence and lower exchange energy terms.[58] For antidot samples with $\boldsymbol{d}$ = 60 nm the magnetic domain structure shows the stripe magnetic domain beside the L-structure,[46, 47, 58,61] as plotted in figure 9b. For samples with $\boldsymbol{d}$ = 75 nm the magnetic domains with L-structure disappeared, and a stripe domain structure prevails, as show in figure 9c. These magnetic strips domain extended for many hexagonal cells. Also, the strip magnetic domain is connected horizontally with high energy super domain wall, HE-SDWs.[58] These HE-SDWs are mainly form when head-to-head or tail-to-tail configurations of the magnetization vector exist and create a high divergence of stray field and high exchange energy density resulting in local out-of-plane easy magnetization direction in these regions.[58] In addition, the in-plane loops for applied field on *x* and *y* direction are approximately the same. By increasing the hole diameter, the magnetic domain structure totally modifies, and the stripe domains tend to disappear. As indicated in figure 9d, the magnetic unit cell consists of five domains in accordance to the five bridges between neighboring holes. The magnetization of the central domain points towards the next nearest neighbor direction, while the other four domains have their magnetization vectors oriented to the next nearest neighbor directions enclosing angles of 60° with respect to the magnetization of the central bridge. As a consequence, the in-plane easy magnetization axis shifts

from near neighbor (*x* direction) to next near neighbor (*y* direction).[61] This magnetic state is supposedly very stable, as it not only minimizes the energy of each single vertex in conformance with the spin-ice rules,[64] but also the interaction energy between neighboring vertices. In addition, it is also responsible for the occurrence of a magnetic component perpendicular to the applied magnetics field[65] (i.e., out of plane direction). Therefore, the induced spin-ice magnetic domain structure causes a reduction of $\boldsymbol{H_{C//}}$ & $\boldsymbol{m_{r//}}$ and an increase of $\boldsymbol{H_{C}}_{\perp}$ and $\boldsymbol{m_{r\perp}}$, as proved with the experimental result where the $\boldsymbol{H_{C//}}$ is decreased above the $\boldsymbol{d_c}$ point.

Conclusions

In summary, the previous results suggest a unified description of the magnetic properties of Ni antidot arrays thin films along the crossover of magnetization from the INP to OOP directions that takes place at the unexpected critical hole diameter of around $\boldsymbol{d_c}$ = 80 nm. The magnetostatic energy associated to the antidot array increases with the antidot hole diameter. When the hole diameter is large enough to counterbalance the energy associated to the magnetic poles on the film surface, the preferred direction of magnetization should change from the INP to OOP direction. The magnetization crossover between the INP and OOP direction has been studied for two antidots densities regimes, LD-AD and HD-AD. At the critical nanohole diameter, the magnetic material between the holes have the same characteristic length $\boldsymbol{R_{crit}} \approx 21$ nm, where the magnetization reversal transition occurs from domain wall nucleation to quasi-uniform magnetization rotation. In addition, the INP effective anisotropy coefficient approaches to zero as there is equivalent energy between the in-plane and out of plane loops. For antidot diameters above $\boldsymbol{d_c}$, a strong effective PMA has been observed. The highest values of effective perpendicular magnetic anisotropy energy density of Ni antidot arrays that have been obtained in this work (1.44 erg/cm^2) are more than (7.5-48)-times stronger than that observed for Ni/Pt (0.18 erg/cm^2) and Ni/Pd (0.03

erg/cm^2) multilayer thin film with PMA, respectively. Furthermore, these findings point toward possibilities to engineer ferromagnetic metal antidots with large perpendicular magnetic anisotropy more than 2-times larger than compared with conventional multilayered systems. Taking into account the long-standing challenge to promote large PMA in small size spintronic devices, antidot based nanomaterials constitute a benchmark for future spintronic information processing technologies and magneto-optic perpendicular recording patterned media.

AUTHOR INFORMATION

Corresponding Author

*Mohamed Salaheldeen (M. Salaheldeen), e-mail: UO253675@uniovi.es & m.salaheldin@science.sohag.edu.eg; and *Victor M. Prida (V.M. Prida), e-mail: vmpp@uniovi.es. Departamento de Física, Facultad de Ciencias, Universidad de Oviedo.

C/ Federico García Lorca nº 18, 33007-Oviedo, Asturias, Spain.

Author Contributions

A. Fernández and V.M. Prida conceive the experiments and supervise the work. V.M. Prida get the funding resources. M. Salaheldeen carried out the experiments. M. Méndez performed the micromagnetic simulations. V. Vega help with the synthesis of samples. M. Salaheldeen write the draft of the manuscript. The final version of the work was written through contributions of all authors, and all of them give their approval to the final version of the manuscript.

ACKNOWLEDGMENT

This work has been financially supported under MINECO research project nº MAT2016-76824-C3-3-R. Common Research Services (SCTs) from University of Oviedo are gratefully recognized.

REFERENCES

(1) Chappert, C.; Fert, A.; Van Dau, F. N. The Emergence of Spin Electronics in Data Storage. *Nat. Mater.* **2007**, *6*, 813–823.

(2) Brataas, A.; Kent, A. D.; Ohno, H. Current-Induced Torques in Magnetic Materials. *Nat. Mater.* **2012**, *11*, 372–381.

(3) Dieny, B.; Chshiev, M. Perpendicular Magnetic Anisotropy at Transition Metal/Oxide Interfaces and Applications. *Rev. Mod. Phys.* **2017**, *89*, 025008.

(4) Monso, S.; Rodmacq, B.; Auffret, S.; Casali, G.; Fettar, F.; Gilles, B.; Dieny, B.; Boyer, P. Crossover from In-Plane to Perpendicular Anisotropy in Pt/CoFe/AlO x Sandwiches as a Function of Al Oxidation: A Very Accurate Control of the Oxidation of Tunnel Barriers. *Appl. Phys. Lett.* **2002**, *80*, 4157.

(5) Ikeda, S.; Miura, K.; Yamamoto, H.; Mizunuma, K.; Gan, H. D.; Endo, M.; Kanai, S.; Hayakawa, J.; Matsukura, F.; Ohno, H. A Perpendicular-Anisotropy CoFeB-MgO Magnetic Tunnel Junction. *Nat. Mater.* **2010**, *9*, 721–724.

(6) Mangin, S.; Ravelosona, D.; Katine, J. A.; Carey, M. J.;Terris, B. D.; Fullerton, E. E. Current-Induced Magnetization Reversal in Nanopillars with Perpendicular Anisotropy. *Nat. Mater.* **2006**, *5*, 210–215.

(7) Emori, S.; Beach, G. S. D. Optimization of Out-of-Plane Magnetized Co/Pt Multilayers with Resistive Buffer Layers. *J. Appl. Phys.* **2011**, *110*, 033919.

(8) Miron, I. M.; Garello, K.; Gaudin, G.; Zermatten, P. J.; Costache, M. V.; Auffret, S.; Bandiera, S.; Rodmacq, B.; Schuhl, A.; Gambardella, P. Perpendicular Switching of a Single Ferromagnetic Layer Induced by In-Plane Current Injection. *Nature* **2011**, *476*, 189–193.

(9) Dai, B.; Kato, T.; Iwata, S.; Tsunashima, S. Temperature Dependence of Critical Current Density of Spin Transfer Torque Switching Amorphous GdFeCo for Thermally Assisted MRAM. *IEEE Trans. Magn.* **2013**, *49*, 4359–4362.

(10) Kaidatzis, A.; Del Real, R. P.; Alvaro, R.; Palma, J. L.; Anguita, J.; Niarchos, D.; Vázquez, M.; Escrig, J.; García-Martín, J. M. Magnetic Properties Engineering of Nanopatterned Cobalt Antidot Arrays. *J. Phys. D. Appl. Phys.* **2016**, *49*, 175004.

(11) Lenk, B.; Ulrichs, H.; Garbs, F.; Münzenberg, M. The Building Blocks of Magnonics. *Phys. Rep.* **2011**, *507*, 107–136.

(12) Yu, H.; Duerr, G.; Huber, R.; Bahr, M.; Schwarze, T.; Brandl, F.; Grundler, D. Omnidirectional Spin-Wave Nanograting Coupler. *Nat. Commun.* **2013**, *4*, 2702.

(13) De, A.; Mondal, S.; Sahoo, S.; Barman, S.; Otani, Y.; Mitra, R. K.; Barman, A. Field-Controlled Ultrafast Magnetization Dynamics in Two-Dimensional Nanoscale Ferromagnetic Antidot Arrays. *Beilstein J. Nanotechnol.* **2018**, *9*, 1123–1134.

(14) Palma, J. L.; Pereira, A.; Álvaro, R.; García-Martín, J. M.; Escrig, J. Magnetic Properties of Fe3O4antidot Arrays Synthesized by AFIR: Atomic Layer Deposition, Focused Ion Beam and Thermal Reduction. *Beilstein J. Nanotechnol.* **2018**, *9*, 1728–1734.

(15) Lange, M.; Van Bael, M. J.; Moshchalkov, V. V.; Bruynseraede, Y. Asymmetric Flux Pinning by Magnetic Antidots. *J. Magn. Magn. Mater.* **2002**, *240*, 595–597.

(16) Filby, E. T.; Zhukov, A. A.; J. de Groot, P. A.; Ghanem, M. A.; Bartlett, P. N.; Metlushko, V. V. Shape Induced Anomalies in Vortex Pinning and Dynamics of Superconducting Antidot Arrays with Spherical Cavities. *Appl. Phys. Lett.* **2006**, *89*, 092503.

(17) Perzanowski, M.; Krupinski, M.; Zarzycki, A.; Dziedzic, A.; Zabila, Y.; Marszalek, M. Exchange Bias in the [CoO/Co/Pd]10Antidot Large Area Arrays. *ACS Appl. Mater. Interfaces* **2017**, *9*, 33250–33256.

(18) Tripathy, D.; Adeyeye, A. O. Perpendicular Anisotropy and Out-of-Plane Exchange Bias in Nanoscale Antidot Arrays. *New J. Phys.* **2011**, *13*, 023035.

(19) Huang, Y. C.; Hsiao, J. C.; Liu, I. Y.; Wang, L. W.; Liao, J. W.; Lai, C. H. Fabrication of FePt Networks by Porous Anodic Aluminum Oxide. *J. Appl. Phys.* **2012**, *111*, 07B923.

(20) Yang, H.; Chen, G.; Cotta, A. A. C.; N'DIaye, A. T.; Nikolaev, S. A.; Soares, E. A.; MacEdo, W. A. A.; Liu, K.; Schmid, A. K.; Fert, A.; Chshiev, M. Significant Dzyaloshinskii-Moriya Interaction at Graphene-Ferromagnet Interfaces Due to the Rashba Effect. *Nat. Mater.* **2018**, *17*, 605–609.

(21) Yang, H.; Vu, A. D.; Hallal, A.; Rougemaille, N.; Coraux, J.; Chen, G.; Schmid, A. K.; Chshiev, M. Anatomy and Giant Enhancement of the Perpendicular Magnetic Anisotropy of Cobalt-Graphene Heterostructures. *Nano Lett.* **2016**, *16*, 145–151.

(22) Liu, C. Y.; Datta, A.; Wang, Y. L. Ordered Anodic Alumina Nanochannels on Focused-Ion-Beam-Prepatterned Aluminum Surfaces. *Appl. Phys. Lett.* **2001**, *78*, 120.

(23) Sun, Z.; Kim, H. K. Growth of Ordered, Single-Domain, Alumina Nanopore Arrays with Holographically Patterned Aluminum Films. *Appl. Phys. Lett.* **2002**, *81*, 3458.

(24) Fournier-Bidoz, S.; Arsenault, A. C.; Manners, I.; Ozin, G. A. Synthetic Self-Propelled Nanorotors. *Chem. Commun.* **2005**, 0, 441–443.

(25) Kim, B.; Park, S.; McCarthy, T. J.; Russell, T. P. Fabrication of Ordered Anodic Aluminum Oxide Using a Solvent-Induced Array of Block-Copolymer Micelles. *Small* **2007**, *3*, 1869–1872.

(26) Zhang, C.; Li, W.; Yu, D.; Wang, Y.; Yin, M.; Wang, H.; Song, Y.; Zhu, X.; Chang, P.; Chen, X.; Li, D. Wafer-Scale Highly Ordered Anodic Aluminum Oxide by Soft Nanoimprinting Lithography for Optoelectronics Light Management. *Adv. Mater. Interfaces* **2017**, *4*, 1601116.

(27) Moreno, J. M. M.; Waleczek, M.; Martens, S.; Zierold, R.; Görlitz, D.; Martínez, V. V.; Prida, V. M.; Nielsch, K. Constrained Order in Nanoporous Alumina with High Aspect

Ratio : Smart Combination of Interference Lithography and Hard Anodization. *Adv. Funct. Mater.* **2014**, *24*, 1857–1863.

(28) Fukuda, H. M. and K. Ordered Metal Nanohole Arrays Made by a Two-Step Replication of Honeycomb Structures of Anodic Alumina. *Science.* **1995**, *268*, 1466–1468.

(29) Prida, V. M.; Salaheldeen, M.; Pfitzer, G.; Hidalgo, A.; Vega, V.; González, S.; Teixeira, J. M.; Fernández, A.; Hernando, B. Template Assisted Deposition of Ferromagnetic Nanostructures: From Antidot Thin Films to Multisegmented Nanowires. *Acta Phys. Pol. A* **2017**, *131*, 822–827.

(30) Salaheldeen, M.; Vega, V.; Ibabe, A.; Jaafar, M.; Asenjo, A.; Fernandez, A.; Prida, V. M. Tailoring of Perpendicular Magnetic Anisotropy in $Dy_{13}Fe_{87}$ Thin Films with Hexagonal Antidot Lattice Nanostructure. *Nanomaterials* **2018**, *8*, 227.

(31) López Antón, R.; Vega, V.; Prida, V. M.; Fernández, A.; Pirota, K. R.; Vázquez, M. Magnetic Properties of Hexagonally Ordered Arrays of Fe Antidots by Vacuum Thermal Evaporation on Nanoporous Alumina Templates. *Solid State Phenom.* **2009**, *152–153*, 273–276.

(32) Han, H.; Park, S. J.; Jang, J. S.; Ryu, H.; Kim, K. J.; Baik, S.; Lee, W. In Situ Determination of the Pore Opening Point during Wet-Chemical Etching of the Barrier Layer of Porous Anodic Aluminum Oxide: Nonuniform Impurity Distribution in Anodic Oxide. *ACS Appl. Mater. Interfaces* **2013**, *5*, 3441–3448.

(33) Rahman, M. T.; Shams, N. N.; Lai, C. H.; Fidler, J.; Suess, D. Co/Pt Perpendicular Antidot Arrays with Engineered Feature Size and Magnetic Properties Fabricated on Anodic Aluminum Oxide Templates. *Phys. Rev. B - Condens. Matter Mater. Phys.* **2010**, *81*, 014418.

(34) Merazzo, K. J.; Leitao, D. C.; Jiménez, E.; Araujo, J. P.; Camarero, J.; Del Real, R. P.; Asenjo, A.; Vázquez, M. Geometry-Dependent Magnetization Reversal Mechanism in Ordered Py Antidot Arrays. *J. Phys. D. Appl. Phys.* **2011**, *44*, 505001.

(35) Wiedwald, U.; Gräfe, J.; Lebecki, K. M.; Skripnik, M.; Haering, F.; Schütz, G.; Ziemann, P.; Goering, E.; Nowak, U. Magnetic Switching of Nanoscale Antidot Lattices Ulf. *Beilstein J. Nanotechnol.* **2016**, *7*, 733–750.

(36) Phuoc, N. N.; Lim, S. L.; Xu, F.; Ma, Y. G.; Ong, C. K. Enhancement of Exchange Bias and Ferromagnetic Resonance Frequency by Using Multilayer Antidot Arrays. *J. Appl. Phys.* **2008**, *104*, 093708.

(37) Vansteenkiste, A.; Leliaert, J.; Dvornik, M.; Helsen, M.; Garcia-Sanchez, F.; Van Waeyenberge, B. The Design and Verification of MuMax3. *AIP Adv.* **2014**, *4*, 107133.

(38) Castán-Guerrero, C.; Herrero-Albillos, J.; Bartolomé, J.; Bartolomé, F.; Rodríguez, L. A.; Magén, C.; Kronast, F.; Gawronski, P.; Chubykalo-Fesenko, O.; Merazzo, K. J.; Vavassori, P.; Strichovanec, P.; Sese, J.; Garcia, L.M. Magnetic Antidot to Dot Crossover in Co and Py Nanopatterned Thin Films. *Phys. Rev. B - Condens. Matter Mater. Phys.* **2014**, *89*,

144405.

(39) Béron, F.; Kaidatzis, A.; Velo, M. F.; Arzuza, L. C. C.; Palmero, E. M.; del Real, R. P.; Niarchos, D.; Pirota, K. R.; García-Martín, J. M. Nanometer Scale Hard/Soft Bilayer Magnetic Antidots. *Nanoscale Res. Lett.* **2016**, *11*, 1182.

(40) Saldanha, D. R.; Dugato, D. A.; Mori, T. J. A.; Daudt, N. F.; Dorneles, L. S.; Denardin, J. C. Tailoring the Magnetic and Magneto- Transport Properties of Pd / Co Multilayers and Pseudo-Spin Valve Antidots. *J. Phys. D. Appl. Phys.* **2018**, *51*, 395001.

(41) D C Leitao, J Ventura, C T Sousa, J M Teixeira, J B Sousa, M Jaafar, A Asenjo, M Vazquez, J M De Teresa, J. P. Araujo. Tailoring the Physical Properties of Thin Nanohole Arrays Grown on Flat Anodic Aluminum Oxide Templates. *Nanotechnology* **2012**, *23*, 425701.

(42) Nguyen, T. N. A.; Fedotova, J.; Kasiuk, J.; Bayev, V.; Kupreeva, O.; Lazarouk, S.; Manh, D. H.; Vu, D. L.; Chung, S.; Akerman, J.; Altynov, V.; Maximenko, A. Applied Surface Science Effect of Flattened Surface Morphology of Anodized Aluminum Oxide Templates on the Magnetic Properties of Nanoporous Co / Pt and Co / Pd Thin Multilayered Films. *Appl. Surf. Sci.* **2018**, *427*, 649–655.

(43) Béron, F.; Pirota, K. R.; Vega, V.; Prida, V. M.; Fernández, A.; Hernando, B.; Knobel, M. An Effective Method to Probe Local Magnetostatic Properties in a Nanometric FePd Antidot Array. *New J. Phys.* **2011**, *13*, 013035.

(44) Fettar, F.; Cagnon, L.; Rougemaille, N. Three-Dimensional Magnetization Profile and Multiaxes Exchange Bias in Co Antidot Arrays. *Appl. Phys. Lett.* **2010**, *97*, 192502.

(45) Jang, Y. H.; Cho, J. H. Morphology-Dependent Multi-Step Ferromagnetic Reversal Processes in Co Thin Films on Crescent-Shaped Antidot Arrays. *J. Appl. Phys.* **2014**, *115*, 063903.

(46) Merazzo, K. J.; Castán-Guerrero, C.; Herrero-Albillos, J.; Kronast, F.; Bartolomé, F.; Bartolomé, J.; Sesé, J.; Del Real, R. P.; García, L. M.; Vázquez, M. X-Ray Photoemission Electron Microscopy Studies of Local Magnetization in Py Antidot Array Thin Films. *Phys. Rev. B - Condens. Matter Mater. Phys.* **2012**, *85*, 184427.

(47) Gawronski, P.; Merazzo, K. J.; Chubykalo-Fesenko, O.; Del Real, R. P.; Vázquez, M. Micromagnetism of Permalloy Antidot Arrays Prepared from Alumina Templates. *Nanotechnology* **2014**, *25*, 475703.

(48) Navas, D.; Hernández- Vélez, M.; Vázquez, M.; Lee, W.; Nielsch, K. Ordered Ni Nanohole Arrays with Engineered Geometrical Aspects and Magnetic Anisotropy. *Appl. Phys. Lett.* **2007**, *90*, 192501.

(49) Lee, J.; Brombacher, C.; Fidler, J.; Dymerska, B.; Suess, D.; Albrecht, M. Contribution of the Easy Axis Orientation, Anisotropy Distribution and Dot Size on the Switching Field Distribution of Bit Patterned Media. *Appl. Phys. Lett.* **2011**, *99*, 062505.

(50) Shaw, J. M.; Russek, S. E.; Thomson, T.; Donahue, M. J.; Terris, B. D.; Hellwig, O.; Dobisz, E.; Schneider, M. L. Reversal Mechanisms in Perpendicularly Magnetized Nanostructures.

Phys. Rev. B - Condens. Matter Mater. Phys. **2008**, *78*, 024414.

(51) Yanagishita, T.; Nishio, K.; Masuda, H. Fabrication of Metal Nanohole Arrays with High Aspect Ratios Using Two-Step Replication of Anodic Porous Alumina. *Adv. Mater.* **2005**, *17*, 2241–2243.

(52) Jaafar, M.; Navas, D.; Asenjo, A.; Vázquez, M.; Hernández-Vlez, M.; García-Martín, J. M. Magnetic Domain Structure of Nanohole Arrays in Ni Films. *J. Appl. Phys.* **2007**, *101*, 09F513.

(53) Krishnan, R.; Lassri, H.; Shiva, P.; Porte, M.; Tessier, M. Magnetic Properties of Ni/Pt Multilayers. *J. Appl. Phys.* **1993**, *73*, 6433.

(54) Jeong, J.-R.; Kim, Y.-S.; Shin, S.-C. Origins of Perpendicular Magnetic Anisotropy in Ni/Pd Multilayer Films. *J. Appl. Phys.* **1999**, *85*, 5762.

(55) Lambert, C. H.; Rajanikanth, A.; Hauet, T.; Mangin, S.; Fullerton, E. E.; Andrieu, S. Quantifying Perpendicular Magnetic Anisotropy at the Fe-MgO(001) Interface. *Appl. Phys. Lett.* **2013**, *102*, 122410.

(56) Inglefield, H. E.; Bochi, G.; Ballentine, C. A.; O'Handley, R. C.; Thompson, C. V. Perpendicular Magnetic Anisotropy in Epitaxial Cu/Ni/Cu/Si (001). *Thin Solid Films* **1996**, *275*, 155–158.

(57) Jungblut, R.; Johnson, M. T.; Aan De Stegge, J.; Reinders, A.; Den Broeder, F. J. A. Orientational and Structural Dependence of Magnetic Anisotropy of Cu/Ni/Cu Sandwiches: Misfit Interface Anisotropy. *J. Appl. Phys.* **1994**, *75*, 6424.

(58) Hu, X. K.; Sievers, S.; Muller, A.; Janke, V.; Schumacher, H. W. Classification of Super Domains and Super Domain Walls in Permalloy Antidot Lattices. *Phys. Rev. B* **2011**, *84*, 024404.

(59) Heyderman, L. J.; Nolting, F.; Backes, D.; Czekaj, S.; Lopez-Diaz, L.; Kläui, M.; Rüdiger, U.; Vaz, C. A. F.; Bland, J. A. C.; Matelon, R. J.; Volkmann, U. G.; Fischer, P. Magnetization Reversal in Cobalt Antidot Arrays. *Phys. Rev. B - Condens. Matter Mater. Phys.* **2006**, *73*, 214429.

(60) Krupinski, M.; Mitin, D.; Zarzycki, A.; Szkudlarek, A.; Giersig, M.; Albrecht, M.; Marszałek, M. Magnetic Transition from Dot to Antidot Regime in Large Area Co/Pd Nanopatterned Arrays with Perpendicular Magnetization. *Nanotechnology* **2017**, *28,* 085302.

(61) Manzin, A.; Bottauscio, O. Micromagnetic Modelling of the Anisotropy Properties of Permalloy Antidot Arrays with Hexagonal Symmetry. *J. Phys. D. Appl. Phys.* **2012**, *45* , 095001.

(62) Kronmüller, H.; Parkin, S. Handbook of Magnetism and Advanced Magnetic Materials; Wiley: New York, 2007; p 695.

(63) Abo, G. S.; Hong, Y. K.; Park, J.; Lee, J.; Lee, W.; Choi, B. C. Definition of Magnetic

Exchange Length. *IEEE Trans. Magn.* **2013**, *49*, 4937–4939.

(64) Ladak,S.; Walton, S. K.; Zeissler, K.; Tyliszczak, T.; Read, D. E.; Branford, W. R.; Cohen, L. F. Disorder-independent control of magnetic monopole defect population in artificial spin-ice honeycombs. *New J. Phys.*, **2012**, 14, 045010.

(65) Farhan, A.; Derlet, P. M.; Anghinolfi, L.; Kleibert, A.; Heyderman, L. J. Magnetic charge and moment dynamics in artificial kagome spin ice. *Phys. Rev. B*. **2017**, 96, 064409.

Table of Contents (TOC)